SCIENCE CHINA
Information Sciences

• REVIEW •

March 2024, Vol. 67, Iss. 3, 131401:1–131401:15
https://doi.org/10.1007/s11432-023-3856-4

Recent progress in single crystal perovskite X-ray detectors

Xiao LIU, Jun REN, Yu-Ang CHEN, Xiangshun GENG, Dan XIE & Tian-Ling REN*

Beijing National Research Center for Information Science and Technology (BNRist), School of Integrated Circuits, Tsinghua University, Beijing 100084, *China*

Received 28 March 2023/Revised 12 June 2023/Accepted 29 August 2023/Published online 19 February 2024

Abstract Perovskites have attracted extensive attention as radiation detection material due to their long carrier diffusion length and lifetime, high absorption coefficient, and flexible manufacturing process. Compared with polycrystalline structures, single crystal perovskites improve the performance of optoelectronic devices due to their low defect state density, better photoelectric characteristics, and chemical stability. Herein, we review the recent progress of single crystal perovskite X-ray detectors. First, we briefly introduced the basic concepts, detection mechanisms, figure of merits of perovskite X-ray detectors, and the preparation methods of single crystal perovskites. Then, we summarized the significant advancements in single crystal perovskite X-ray detectors in recent times. Finally, we discussed the critical challenges and some practicable solutions for developing high-performance X-ray detectors.

Keywords single crystal perovskites, carrier transport, radiation detection, X-ray detectors, X-ray imaging

1 Introduction

Perovskites, named by the Russian mineralogist Count Lev Aleksvich von Perovski, are compounds with a crystal structure similar to that of $CaTiO_3$ [1,2]. Depending on the ionic radii of A, B, and X elements, these materials with the formula ABX_3 could change from cubic phase to tetragonal or orthorhombic phase [3–5]. The tolerance factor (t) can be used to predict the stability of the perovskite lattice [6, 7] and is given by the following equation:

$$t = \frac{r_{\mathrm{A}} + r_{\mathrm{X}}}{\sqrt{2}\,(r_{\mathrm{B}} + r_{\mathrm{X}})},$$

where r_{A}, r_{B}, and r_{X} represent the ionic radii of the A, B, and X elements, respectively. Empirically, nonperovskite structures are formed when $t \leqslant 0.8$ [8] while $t > 1$ leads to hexagonal structures and $0.8 < t < 1$ results in perovskites. Additionally, the octahedral factor, i.e., the ratio of the ionic radius of B site to A site, provides another discriminant rule regarding the octahedral stability and is typically found in the range of 0.44–0.9 [7]. Perovskites can also exist in a layered form, where the ABX_3 structure is separated by thin sheets of spacer material R. This type of layered perovskites can be expressed using the formula $R_2A_{n-1}B_nX_{3n+1}$ and are usually referred as 2D perovskites.

X-ray detection plays an important role in various applications, including medical imaging, industrial quality control, safety screening, and scientific inspection. In the past few decades, semiconductor radiation detectors are primarily based on cadmium zinc telluride ($Cd_{1-x}Zn_xTe$, CZT), silicon (Si), and amorphous selenium (α-Se) [9–13]. These materials have been extensively studied and have also yielded impressive results, but some undesirable issues limit their applicability for high-performance requirements, particularly in precision medicine, nuclear science, and other fields. For example, despite many efforts, the production cost of CZT single crystals remains quite high [14]. At room temperature, high-purity germanium (HPGe) and mercury iodide (HgI_2) exhibit high leakage current and low resistivity [15]. Detectors based on α-Se or Si lack sufficient sensitivity due to their low mobility-lifetime product and small

* Corresponding author (email: RenTL@tsinghua.edu.cn)

atomic number Z [16]. This is because the attenuation coefficient μ of X-ray is strongly dependent on Z as $\mu = \rho Z^4/AE^3$ [17], where ρ, A, and E represent the density, atomic mass of sensing material and energy of X-ray, respectively.

Metal halide perovskites are a promising candidate as light harvest material in photoelectric devices [18–25] and radiation detectors [26–32] due to their excellent optoelectronic properties, including large and balanced carrier mobilities [33–35], long carrier diffusion lengths [36], long carrier lifetimes [37], large X-ray attenuation coefficients [38], tunable bandgaps [39, 40], small exciton binding energies [41], shallow point defect physics [42], and simple fabrication techniques [43, 44]. Perovskites, especially the single crystalline ones, have been extensively studied for high-performance X-ray detection because they have fewer grain boundaries and lower trap densities and lower scattering probability than those of polycrystals, thereby providing better optoelectronic properties and stabilities [30, 45].

This review begins with an overview of the fundamentals and synthetic routes of single crystal perovskites. Then, the recent advancements in X-ray detectors based on single crystal perovskite are summarized. Finally, an outlook and future challenges of perovskite photodetectors are discussed.

2 Fundamentals

2.1 Operating mechanism of X-ray detection

X-ray photons can interact with matter through several mechanisms [7], depending on the energy of X-ray photons and atomic number of matter. Photoelectric effect absorption dominates when the energy of X-ray photons is less than approximately 100 keV and larger than the shell binding energy of atoms. The incident photon and its energy will be absorbed by the atom, producing an ionized atom in its higher energy state and ejecting a photoelectron from the inner shell of the atom. The ionized atom would later return to its ground state by emitting characteristic X-ray photons or Auger electrons. Compton scattering (incoherent scattering) occurs when the energy of photons is over about 30 keV. The incident photon will collide with the atom and transfer a part of its energy to the atom, resulting in a lower-energy X-ray photon and a recoil electron.

The ejected electrons, including photoelectrons, Auger electrons and recoil electrons, continue to process high energy. Thus, as they pass through the semiconductor, more free electrons and holes are generated by ionization and then relax to the bottom of the conduction band or the top of the valance band through individual collision or collective motions. In perovskite X-ray detectors, the electron-hole pairs are converted to electrical output signals in two ways [46–48], as shown in Figure 1. For direct detectors, the electron-hole pairs are collected by electrodes as signals under the influence of an external or built-in electric field. For indirect detectors, the electron-hole pairs first recombine and emit scintillation light, which is then captured and converted into electrical signals using UV or visible light photodetectors. The differences in performance between these two types of detectors are generally due to the extra step of scintillation light detection and the self-absorption effect in indirect X-ray detectors, where emitted photons are reabsorbed by the crystal itself [49]. In general, direct X-ray detectors have a shorter response time, higher spatial resolution, and simpler device structure, while indirect X-ray detectors possess better operational stability, lower manufacturing cost, and no additional requirement of external bias [50, 51].

To develop a good direct X-ray detector, the sensing material needs to satisfy the following requirements [29]:

- Large atomic number (Z) for larger photon cross-section area of photoelectric absorption and scattering.
- Moderate band gap and low electron-hole ionization energy to obtain more photogenerated electron-hole pairs.
- High bulk resistivity to minimize the leakage current.
- A high intrinsic $\mu\tau$ (mobility-lifetime) product.
- Large crystals with low defect density and sufficient thickness.

2.2 Performance evaluation standards of X-ray detectors

The sensitivity (S) and detection limit (or the limit of detection, LoD) are the most-used evaluation parameters for X-ray detectors. The sensitivity represents the ability of the detector to convert X-ray

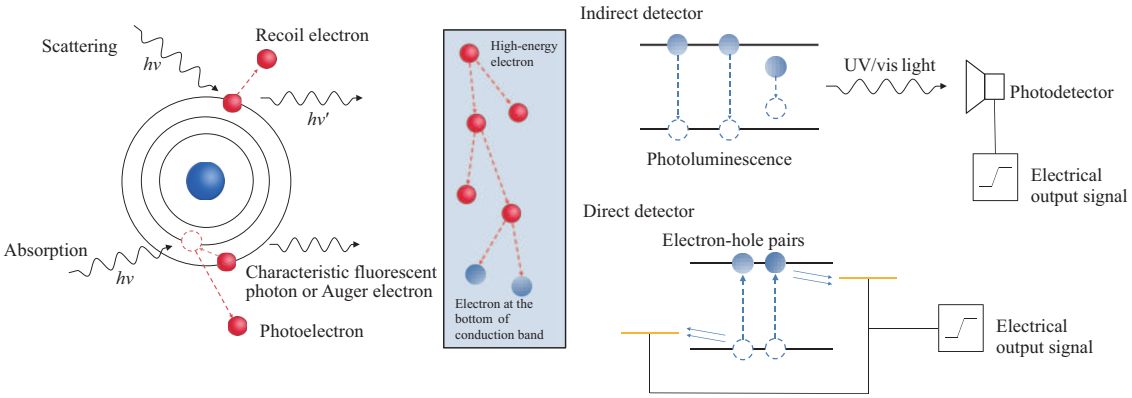

Figure 1 (Color online) Schematic of X-ray detection.

Table 1 The key parameters of X-ray detectors

Parameters	Notation	Unit	Definition
Sensitivity	S	$\mu C/(Gy_{air}\cdot cm^2)$	Collected charge per unit area per unit of radiation exposure.
Detection limit	LoD	Gy_{air}/s	Dose rate yielding an SNR value of 3.
Gain factor	G	–	Ratio of signal current to theoretical current induced by impact ionization; it can be understood as the charge collection efficiency (CCE).
Response time	–	s	Rise and decay times needed for the signal current to vary to a certain value during the on-off cycles.
Dark current drift	D	$A/(cm\cdot s\cdot V)$	Dark current variation caused by ion migration.
Spatial resolution	–	lp/mm	Number of distinguishable line pairs (alternating black and white lines) per millimeter.

photons to electronic signals, as shown in the following equation [52–54]:

$$S = \frac{I_R - I_{\rm dark}}{D \cdot A},$$

where I_R and $I_{\rm dark}$ are the output current under irradiation and in darkness, respectively; D is the X-ray radiation dose rate (unit: $Gy_{air}\cdot s^{-1}$); and A is the effective area of the detector. A high-sensitivity detector could generate large electronic signals at a low dose rate, which is particularly important for medical imaging, such as computed tomography, for reducing the risk of radiation exposure to patients.

LoD is defined as the lowest dose rate while maintaining the signal-to-noise ratio (SNR) larger than a specific value, whose value is usually taken as 3 based on the definition of the International Union of Pure and Applied Chemistry [55, 56]. To reduce LoD to a desirable level, one should simultaneously accomplish low dark current, high sensitivity, and small noise signal.

The stability of X-ray detectors can be evaluated using dark current drift D (same notation as dose rate), which is the dark current variation under certain external electric fields over unit time. It can be expressed as follows [57]:

$$D = \frac{J_t - J_0}{t \cdot E},$$

where t is the duration, E is the electric field, and J and J_t are the current densities at the beginning and ending points. The dark current drift D is used to investigate the baseline drift caused by the ion migration of X-ray detectors.

The response time is a universal parameter for sensors and is defined as the rise and decay times of output signals during input switching. The response time of X-ray detectors is affected by various factors, such as the mobility of carriers and the size of devices.

X-ray detectors are widely used in imaging systems for medical diagnosis or safety screening; hence, spatial resolution is an important parameter for evaluating their performance. It is usually defined as the number of distinguishable line pairs (alternating black and white lines) per millimeter, stated in a unit of "lp/mm". Table 1 lists these key parameters of X-ray detectors.

3 Crystal growing method

For X-ray detectors, the thickness of a single crystal is advantageous for obtaining high attenuation coefficients and charge collection efficiency. Therefore, the synthetic routes of perovskites for X-ray detection primarily focus on single crystals rather than thin films. This section summarizes several solution-based growing methods of single crystal perovskites, including solvent evaporation, inverse temperature crystallization (ITC), and antisolvent vapor-assisted crystallization. These solution-based methods can produce high-quality crystals with large carrier mobility and lifetime or more complicated structures, such as heterojunctions and patterned microarrays [58,59], which can be beneficial to the array integration of the X-ray detectors. The Bridgman method, commonly used for growing large-size perovskite single crystals, is briefly discussed at the end of this section.

3.1 Solvent evaporation

Solvent evaporation is a solution-based method of growing crystals, wherein desired compounds are first dissolved in solvents, and then the solvents are evaporated slowly. It is probably the easiest solution growth method for single crystal perovskites [29]. First, a precursor solution is prepared by dissolving precursors with a certain molar ratio in high boiling point polar solvents like γ-butyrolactone (GBL), *N*,*N*-dimethylformamide (DMF), dimethyl sulfoxide (DMSO) or *N*-methyk-2-pyrrolidone (NMP) [60]. Then as the solvents evaporate, the concentration of perovskites increases and the mixed solution becomes supersaturated, resulting in the nucleation and growth of crystals.

Although solvent evaporation seems relatively simple, growing large-size and high-quality perovskite single crystals remains challenging. Recrystallization, secondary nucleation, and inconsistent evaporation rate at the liquid-solid or liquid-air interfaces would considerably affect the size, shape, and crystallinity of perovskites [61,62]. Moreover, this method is incompatible with high-throughput manufacturing processes due to its time consumption and cumbersome cutting or transfer procedure typically required for device fabrication. Corzo et al. [63] reported a universal strategy that could be used to fabricate various single crystal perovskite arrays with precise positioning, size, and shape. As shown in Figure 2(a), droplets of perovskite precursors are cast on the functionalized SiO_2 substrates, which have been then treated with octadecyltrichlorosilane (OTS) to produce a nonpolar hydrophobic end-tail self-assembled monolayer. As the liquid droplet dries and shrinks, it becomes supersaturated and initiates the nucleation process within a time scale of minutes. By introducing a cosolvent that has a high boiling point and low solubility towards the perovskite precursors, the nucleation is more likely to occur in the bulk of the droplet rather than at its edges. The droplets remain "unattached" to the functionalized surface during the drying process (Figure 2(b)), ensuring fewer grains to be formed, and even single crystals while the concentration of the cosolvent is carefully chosen (Figures 2(c) and (d)). This modified growing method could produce small single crystal perovskite arrays and precisely control the final size and position of the crystals (Figures 2(e)–(g)).

3.2 Antisolvent method

In 2014, Cheng et al. [64] and Seok et al. [65] developed a fast deposition-crystallization procedure for perovskites by using two kinds of solvents in the solvent-solute system. One of the solvents can dissolve many solutes, whereas the other has poor solubility for the solute. When the second solvent, i.e., the antisolvent, enters the saturated solution system, it will rapidly reduce the solubility of the solute in the mixed solvent, thereby promoting fast nucleation and growth of the crystals. Alternatively, the antisolvent could dramatically accelerate the crystallization of perovskites [66, 67]. This fast crystallization method is called the antisolvent method.

In 2015, Shi et al. [68] reported an antisolvent vapor-assisted crystallization method that could grow high-quality, millimeter-sized $MAPbX_3$ single crystal. The antisolvent dichloromethane (DCM), in which precursors are completely insoluble, was slowly evaporated and diffused into the solution. This method has also been used to successfully synthesize other types of perovskite single crystals, including $CsPbBr_3$ [69,70] $FAPbI_3$ [71], and $(NH_4)_3Sb_2X_9$ [72]. Kim et al. [73] reported a modified antisolvent process, in which antisolvent is added during spinning via spraying instead of dripping. This modified method is well-suitable for fabricating large-area devices. Furthermore, Peng et al. [74] reported an antisolvent inkjet printing method for directly patterning perovskite single crystals on any substrates without requiring any surface modifications. As shown in Figure 3(a), a dual-port nozzle drips precursor and antisolvent

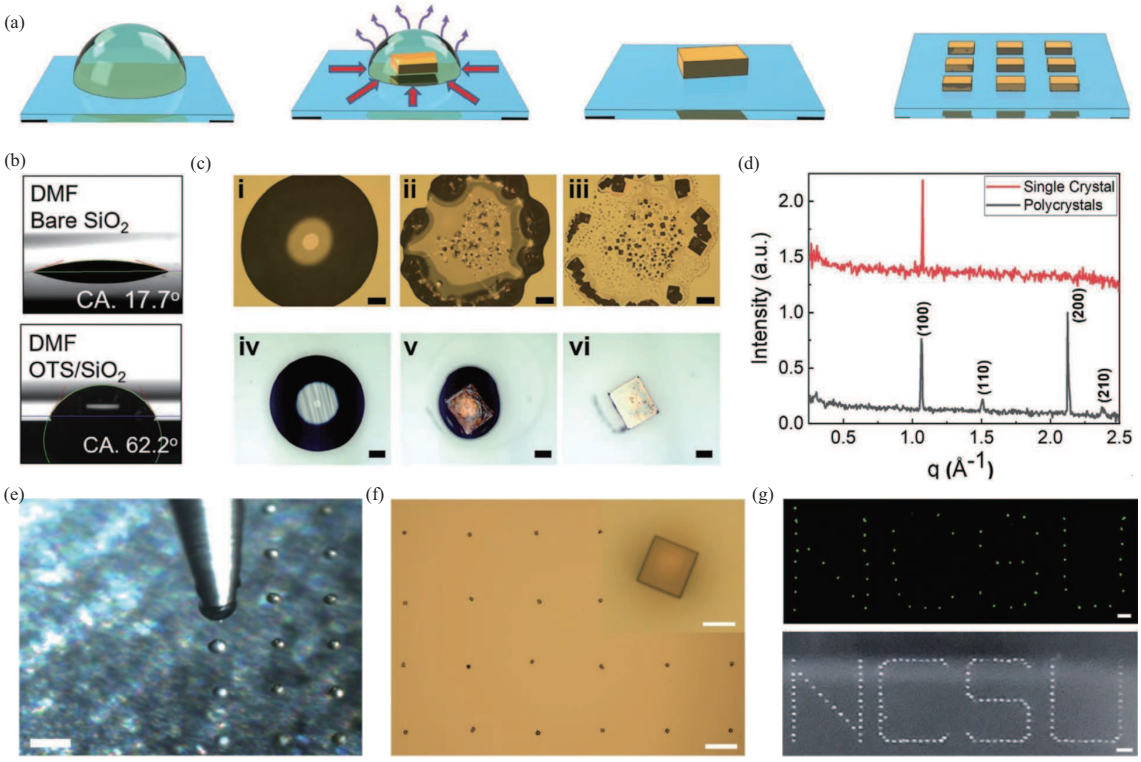

Figure 2 (Color online) A modified evaporation-based single crystalline perovskite synthesis method. (a) Schematic of the conversion from precursor droplet to a single crystal. (b) The contact angle of DMF over bare silica vs. OTS-terminated silica. (c) The drying process on bare silica (i–iii) and OTS-terminated silica (iv–vi). (d) The μWAXS patterns of printed $CH_3NH_3PbBr_3$ ($MAPbBr_3$) single crystal and polycrystals. (e) Microprinting of $MAPbBr_3$ single crystal arrays. (f) Printed arrays with a center-to-center distance of 200 μm. Scale bars: 100 μm. (g) Fluorescence image of the printed pattern and photograph image of a larger similar pattern formed using $MAPbBr_3$ single crystal. Scale bars: 100 μm and 1 mm, respectively [63] © 2022 Wiley.

droplets on the substrate, leading to the formation of a crystal nucleus near the liquid interface between the two droplets, whose size increases gradually with time. Single crystalline perovskite with a grain size of up to 500 μm is observed in their research. This modified method could avoid the coffee-ring effect (Figure 3(b)), which allows producing direct patterns with precise position control and even growing crystal along the z-axis (Figure 3(c)).

3.3 ITC

The solubility and saturated concentration of a solute vary with changes in temperature. Therefore, it is possible to synthesis crystals using the temperature gradient method. ITC is a crystal-growing method driven by the differences in solubility at different temperatures. In 2015, Kadro et al. [75] found inverse solubility of $MAPbI_3$ in GBL at high temperatures (Figure 4(a)) and presented a facile solution-based method for growing freestanding crystals. Saidaminov et al. [76] soon demonstrated that this method can be used to obtain high-quality $MAPbX_3$ single crystals at a lesser time than previous methods by several orders of magnitude. A similar phenomenon of abnormal solubility has also been observed with other solvents, including DMSO and DMF, for synthesizing $MAPbX_3$ [77]. With an increase in temperature, the solubility of perovskite decreases, triggering its nucleation and crystallization. The ITC method permits rapid, high-quality, large-size, and shape-controlled growth of single crystalline perovskites.

Wei et al. [78] reported a modified reverse-solubility method for monolithically integrating $MAPbBr_3$ single crystals on a silicon wafer. As shown in Figure 4(b), a layer of APTES (brominated 3-aminopropyl triethoxysilane) is primarily added to the substrate to react with dangling Si-O-Si bonds and form an NH_2-terminated molecule layer. A preseeded $MAPbBr_3$ single crystal with dimensions of less than 300 μm was introduced onto the wafer, modified with NH_3Br-terminated molecules, and grown to a millimeter-sized single crystal by immersing the Si substrate in $MAPbBr_3$/DMF solution. Wang et al. [79] used a self-supply approach to synthesize high-quality $MAPbI_3$ with a size larger than 4 cm. The precursor solution is contained in an H-like apparatus (Figure 4(c)), where one of the cylinders (Cylinder A) is

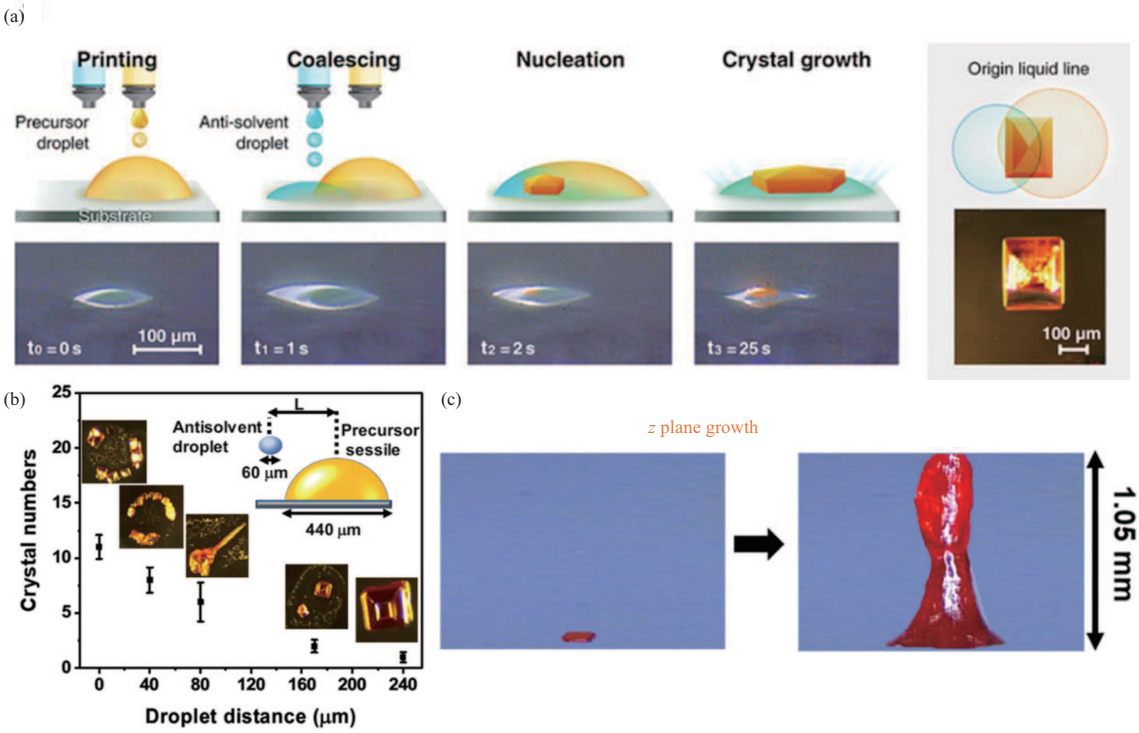

Figure 3 (Color online) An antisolvent inkjet printing method for directly patterning perovskite single crystals. (a) Schematic of the crystallization process of droplets on a glass substrate via a dual-port inkjet; (b) variation of crystal numbers with offset distance; (c) crystal growth along the vertical direction [74] © 2022 American Chemical Society.

kept at a low temperature while the other (Cylinder B) is heated slowly. The seed crystal in Cylinder A will maintain continuous, stable, and controllable growth. The raw materials in Cylinder B can be dissolved until saturation and transported to Cylinder A through natural fluid convection driven by the concentration gradient. Gao et al. [80] prepared a series of mixed-cation lead mixed halide $FA_{1-y}Cs_yPbI_{3-x}Br_x$ perovskite single crystals using the ITC method (Figure 4(d)). Seed crystals are first placed into fresh precursor solutions and then slowly heated to 120°C, which then grows to centimeter-sized large single crystals. These perovskites exhibit good environmental stability for high-energy X-ray detectors.

3.4 Bridgman method

Bridgman method which is based on controlling the temperature gradient to achieve crystal growth, has been extensively used for single crystal growth [81]. Initial samples, usually powders or polycrystalline material, are heated above their melting point in the hot zone of the furnace and then slowly moved to a cold zone. Crystal growth occurs at the interface between the melt and a single crystalline seed, driven by the temperature difference between the hot and cold zones. The as-grown single crystal ingot will follow the specified crystallographic orientation defined by the seed. The Bridgman method requires high temperature, high vacuum conditions, and days of time for growth, but it could avoid undesirable impurity defects from the precursors or soluble organic molecules, which are present in solution-based techniques, ensuring the consistency of the actual compositions of the as-grown crystals with the theoretical formulas.

As shown in Figure 5, Zhang et al. [82] reported centimeter-sized bulk $CsPbBr_{3-n}X_n$ single crystal perovskites using a modified Bridgman method in 2021. Raw materials are first synthesized in a sealed silica ampoule at 600°C–700°C for 24 h to obtain compact polycrystals. The polycrystals are then transferred into a vertical Bridgman furnace under vacuum, heated at 550°C–650°C for 6 h and slowly moved downwards to the cold zone of the furnace at a speed of 0.2–1 mm/h. The centimeter-sized bulk single crystals showed high stability and tunable optoelectronic properties, indicating a novel approach for synthesizing high-performance X-ray image sensors.

Solvent evaporation and antisolvent crystallization are the simplest methods for growing perovskite single crystals and are suitable for various perovskites. However, these methods have a slow growth rate,

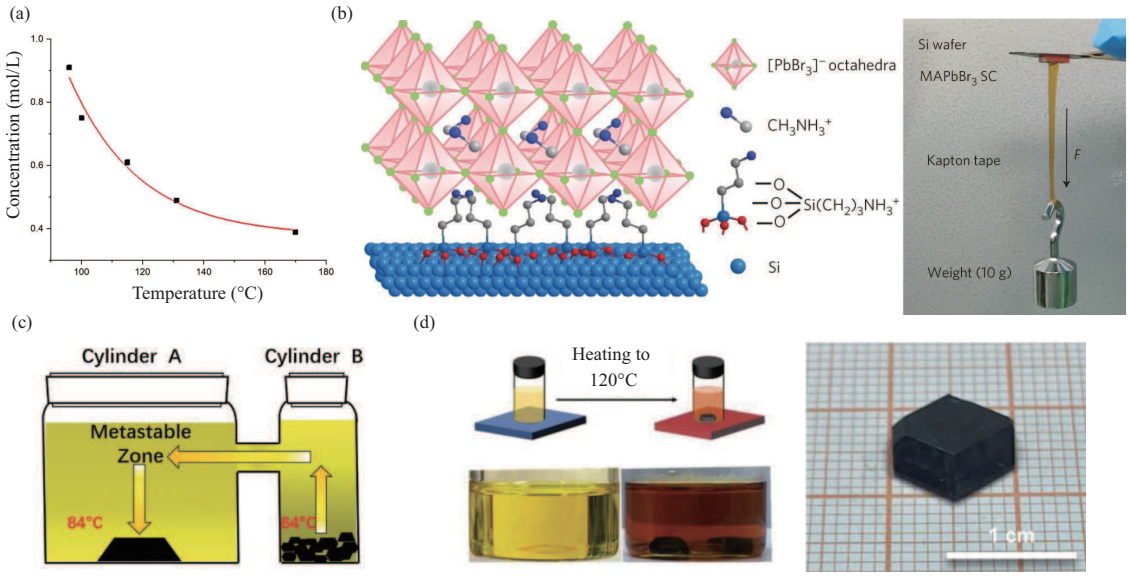

Figure 4 (Color online) (a) Inverse solubility of $MAPbI_3$ in GBL [75]; (b) directly integrated single crystal perovskites on silicon substrate by introducing an NH_2-terminated molecule layer [78] © 2017 Springer Nature; (c) continuous growth of perovskite in H-shape apparatus using ITC [79] © 2020 Wiley; (d) growth of radiation-stable perovskite single crystals using ITC [80] © 2021 Wiley.

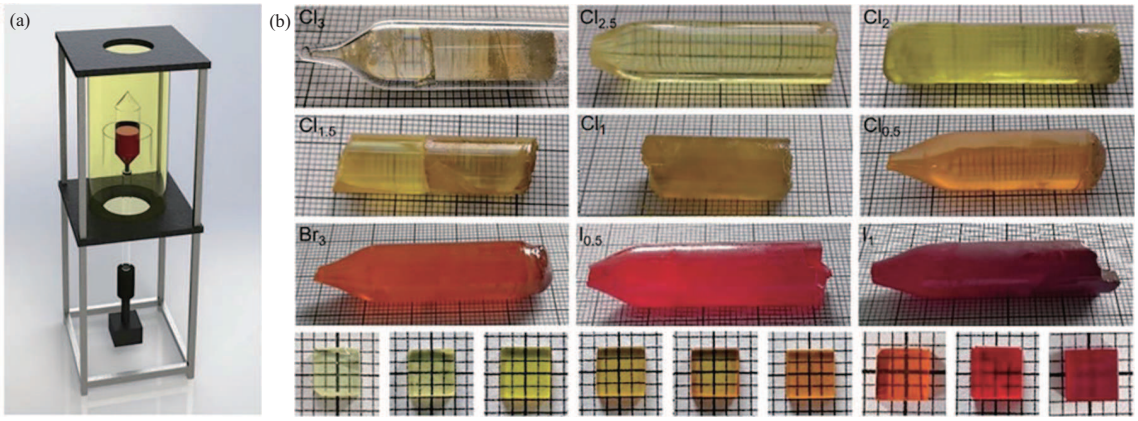

Figure 5 (Color online) Modified Bridgman method of single crystalline perovskites. (a) Diagram of Bridgman furnace; (b) as-grown bulk $CsPbBr_{3-n}X_n$ crystals [82] © 2021 Royal Society of Chemistry.

Table 2 Relative merits of various perovskite growing methods

Growing method	Mechanism	Advantages	Limitations
Solvent evaporation	Evaporation of the solvent.	Simple	Time-consuming and undesired nucleation centers.
Antisolvent method	Solubility change in the mixed solution after adding the antisolvent.	Simple, universal	Time consuming and hard to deposit on some substrates due to the high nucleation energy of the smooth surface.
Inverse temperature crystallization	Temperature-induced decrease in the solubility.	Fast, universal	Disorders, defects, and cracks caused by temperature convection and phase transitions.
Bridgman method	Phase change from liquid to solid.	Large-size and high-quality single crystals	Time-consuming and high operating temperature.

typically taking days of time. The temperature gradient method could grow perovskites in less time, but undesirable defects and cracks would form throughout the crystal phase transitions and thermal convections when the temperature varies. The Bridgman method is not a solution-based method and is expensive as it requires an experimental setup equipped with high vacuum and temperature conditions. But it could prepare large-size and high-quality single crystals. The relative merits of these methods are summarized in Table 2.

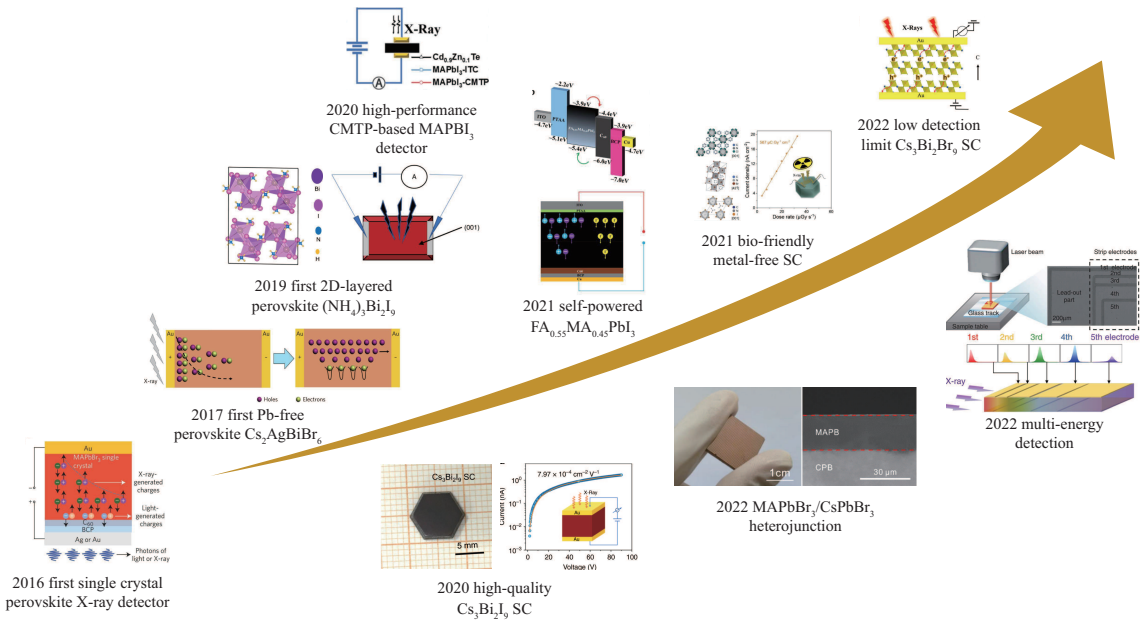

Figure 6 (Color online) Representative studies of single crystal perovskite X-ray detectors in recent years [86] © 2016 Nature; [87] © 2017 Nature; [88] © 2019 Nature; [79] © 2020 Wiley; [89] © 2020 Nature; [90] © 2021 Wiley; [91,92] © 2022 ACS Publication; [93] © 2022 Nature.

4 Single crystal perovskite X-ray detectors

X-ray detectors are widely used in medical diagnosis, industrial monitoring, scientific research, and security screening [47, 83, 84]. Perovskites are a promising candidate for constructing high-performance detectors due to their high average atomic number, suitable bandgap, low trap density, large bulk resistivity, high sensitivity, and stability. Besides, single crystal perovskites usually perform better because the point defects, impurities, dislocations, and grain boundaries in polycrystals could result in nonradiative recombination and material degradation, deteriorating the performance of the device [85]. Figure 6 [79,86–93] summarizes some of the representative studies of single crystal perovskite X-ray detectors.

Wei et al. [86] reported the first sensitive X-ray detectors made of 2-mm-thick $MAPbBr_3$ single crystals. In their antisolvent method, the $PbBr_2$/MABr molar ratios were modified from 1.0 to 0.8 to eliminate the ill effects caused by different solubility of precursors in DMF and grow high-quality single crystals of strict stoichiometry and less surface impurities. Moreover, surface passivation of perovskite by UV-O_3 effectively reduced the high density of surface defects in the as-grown crystals, resulting in improved charge extraction efficiency of the device. The X-ray detector shows a small dark current density of 29 $nA{\cdot}cm^{-2}$ at -0.1 V bias, high sensitivity of 80 $\mu C{\cdot}Gy_{air}^{-1}{\cdot}cm^{-2}$ and a low detectable dose rate of 0.5 $\mu Gy_{air}{\cdot}s^{-1}$. Due to the large charge carrier mobility of $MAPbBr_3$ single crystals, the detector shows a relatively short response time of 216 μs and 1.1 ms for the 1-mm- and 2.6-mm-thick samples respectively, which is in good agreement with the transit times of charge carriers (200 μs and 1.3 ms) for these devices. These researchers [78] also reported Si-integrated single crystal perovskites for highly sensitive X-ray imaging, demonstrating a sensitivity of 2.1×10^4 $\mu C{\cdot}Gy_{air}^{-1}{\cdot}cm^{-2}$ under 8 keV irradiation. Pan et al. [87] reported Pb-free perovskite X-ray detectors made of $Cs_2AgBiBr_6$ single crystals with a minimum detectable dose rate of 59.7 $nGy_{air}{\cdot}s^{-1}$. Here, authors utilized thermal annealing and surface treatment to improve the carrier transport and decrease the surface trap density proving that lead-free perovskites can achieve satisfactory device performance compared to their lead counterparts. Zhuang et al. [88] used 2D layered perovskite $(NH_4)_3Bi_2I_9$ single crystal for producing highly sensitive X-ray detectors. This perovskite is grown using a low-temperature solution method and could be easily dissected from the (001) surface. A 1.5-mm-thick single crystal detector shows high sensitivity along the parallel direction of 8.2×10^3 $\mu C{\cdot}Gy_{air}^{-1}{\cdot}cm^{-2}$ with low LoD of 55 $nGy_{air}{\cdot}s^{-1}$ and good stability after 60 days in ambient air.

Single crystal perovskites have shown great potential for detection and imaging, but there is still a long way to go before they can be used in practical applications. Therefore, many studies are proposed

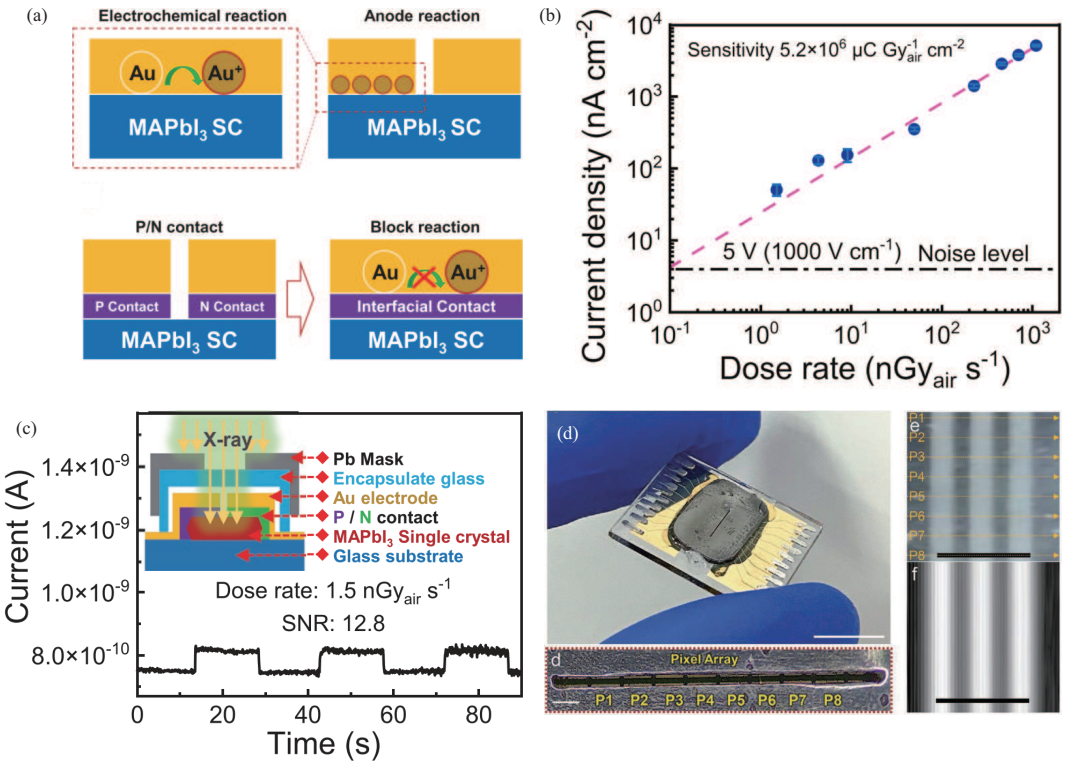

Figure 7 (Color online) Eliminate the interfacial reaction and improve the performance of the perovskite X-ray detector. (a) Electrochemical reaction at the anode in devices without and with interfacial layers; (b) the current density of the X-ray detector varies with the incident dose rate; (c) schematic of an encapsulated device; (d) the photo of the linear detector arrays. Scale bars: 1 cm [16] © 2021 Wiley.

to solve theoretical and technical problems, such as improving LoDs, optimizing chemical composition and device structure, and reducing cost. One approach to solve these issues is developing and improving the preparation methods to get better-quality perovskite single crystals. Zhang et al. [89] developed a nucleation-controlled solution method and grew high-quality $Cs_3Bi_2I_9$ single crystals. The precursor solution was carefully filtered and recrystallized at 80°C for at least 24 h. Almost all extraneous nucleation seeds, including dust, bubbles, and particulates, are removed through these solution refinement processes. A high $\mu\tau$ product of 7.97×10^{-4} $cm^2 \cdot V^{-1}$ is measured, leading to a high sensitivity of 1.65×10^3 $\mu C \cdot Gy_{air}^{-1} \cdot cm^{-2}$ and a LoD of 130 $nGy_{air} \cdot s^{-1}$. Li et al. [92] modified the Bridgman technique and successfully grew inch-sized $Cs_3Bi_2Br_9$ single crystals with high quality, exhibiting low trap density, high ion activation energy, a bulk resistivity of 1.41×10^{12} $\Omega \cdot cm$ and a $\mu\tau$ product of 8.32×10^{-4} cm^2. The detector showed excellent hard X-ray detection performance with a sensitivity of 1705 $\mu C \cdot Gy_{air}^{-1} \cdot cm^{-2}$, a LoD of 0.58 $nGy_{air} \cdot s^{-1}$, and an ultralow dark current drift of 2.8×10^{-10} $nA \cdot cm^{-1} \cdot s^{-1} \cdot V^{-1}$.

Introducing additional layers and changing the structure could improve the performance of X-ray detectors. To further improve the LoD and performance at a low dose rate of the detector, Song et al. [16] introduced C_{60}/BCP and MoO_x as P/N contact layer into the $MAPbI_3$ detector (Figure 7(a)). The additional layer can isolate the Au electrodes, build a high interfacial contact barrier, eliminate the electrochemical reaction, and suppress the dark current by three orders of magnitude (Figure 7(b)). The detector showed high sensitivity of 5.2×10^6 $\mu C \cdot Gy_{air}^{-1} \cdot cm^{-2}$ and a record low LoD down to 0.1 $nGy_{air} \cdot s^{-1}$. Superior environmental stability is achieved by encapsulating the device with glass and a Pb mask (Figure 7(c)). The signal current exhibits negligible degradation in ambient condition with an average humidity of about 60% for 1600 h. They built an X-ray imaging prototype based on linear $MAPbI_3$ detector arrays (Figure 7(d)), showing a clear and high-contrast image of a standard Pb test-pattern plate.

Substituting the methyl ammonium ($CH_3NH_3^+$, MA) for larger organic cations, such as ethyl ammonium ($C_2H_8N^+$, EA) [94], guanidinium ($C(NH_2)_3^+$, GA) [95], and dimethylammonium ($(CH_3)_2NH_2^+$, DMA) [96] could reduce free energy and the degree of octahedral tilting of the PbX_6-framework, resulting in higher crystal symmetry, improved material stability, and longer lifetime of charge carriers.

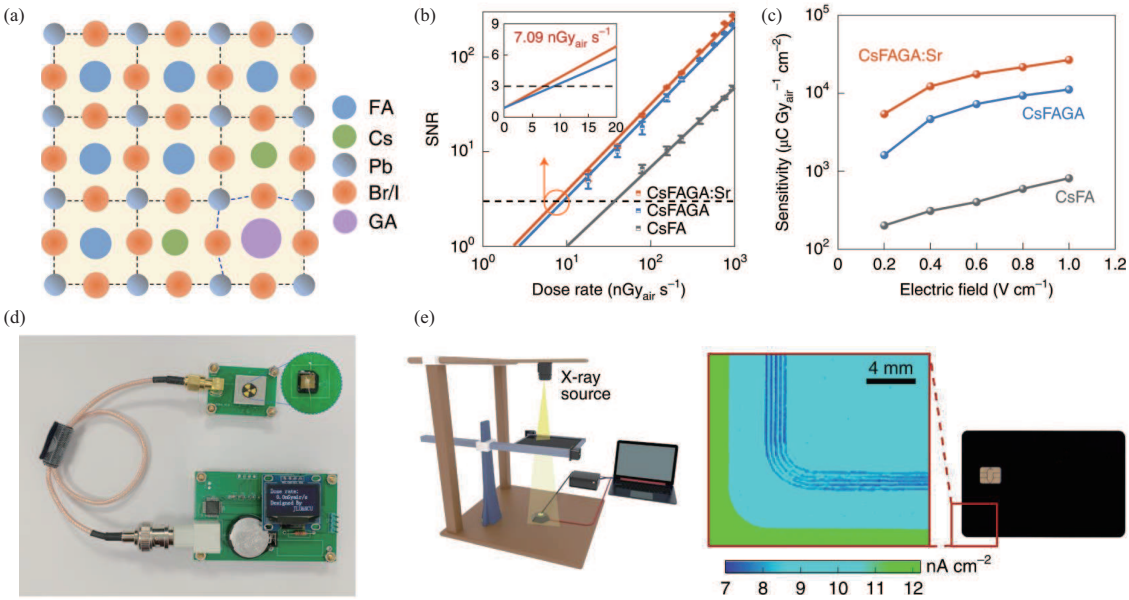

Figure 8 (Color online) Stable and sensitive X-ray detector through synergistic strain engineering. (a) Synergistic doping of GA and FA in $CsPbX_3$ to relax local tensile strain; (b) LoD of CsFA, CsFAGA and CsFAGA:Sr X-ray detectors; (c) sensitivity of X-ray detectors under different electric fields; (d) the prototype of a portable X-ray monitor; (e) X-ray imaging system and an X-ray image of a bank card [97] © 2022 Nature.

Wu et al. [90] incorporated FA^+ cations into the $MAPbI_3$ single crystals and developed a self-powered X-ray detector. This device could operate under zero bias and exhibit low noise and large photoresponse. The experimental results showed a good sensitivity of 8.7×10^4 $\mu C \cdot Gy_{air}^{-1} \cdot cm^{-2}$ and a LoD of 27.7 $nGy_{air} \cdot s^{-1}$. Kishimoto et al. [95] developed $GAMAPbI_3$ based X-ray detectors with a $\mu\tau$ product of 1.3×10^{-2} $cm^2 \cdot V^{-1}$, high sensitivity of 2.3×10^4 $\mu C \cdot Gy_{air}^{-1} \cdot cm^{-2}$ and low detectable dose rate of 16.9 $nGy_{air} \cdot s^{-1}$. Jiang et al. [97] used a synergistic strain engineering strategy to shift the A-site cation from Cs to FA and GA and B-site cation from Pb to Sr in a mixed halide perovskite (Figure 8). The dual-site-doped perovskite single crystal realized a sensitivity of 2.6×10^4 $\mu C \cdot Gy_{air}^{-1} \cdot cm^{-2}$ under low field and a LoD of 7.1 $nGy_{air} \cdot s^{-1}$. This material design strategy could improve device performance and long-term stability simultaneously, providing new insights into other commercial perovskite optoelectronic applications and gamma-ray spectrum acquisition.

Developing heterostructures could be another strategy for improving the performance of devices. It could integrate the optoelectronic features of two materials, suppress the dark current and dark current drift, and enable self-powered detection owing to the built-in electric field [98,99]. Cui et al. [91] reported a facile liquid-phase epitaxial method and developed large-area $MAPb(Br, I)_3/CsPbBr_3$ single crystal heterojunction, which showed robust and uniform X-ray imaging performance with high sensitivity of 2.0×10^5 $\mu C \cdot Gy_{air}^{-1} \cdot cm^{-2}$ and a LoD of 96 $nGy_{air} \cdot s^{-1}$. Zhang et al. [100] developed centimeter-sized $(BA)_2CsAgBiBr_7/Cs_2AgBiBr_6$ single crystal heterocrystals using an insitu epitaxial solution-processing method. The new $(BA)_2CsAgBiBr_7$ crystal could fill the microgaps between the two solids to achieve strong interfacial adhesion, and it also exhibited a type II band alignment that favors carrier separation. Combining 3D crystal with its 3D counterpart could suppress ion migration and large bulk resistance, attributing to the built-in electric potential. The self-driven X-ray detector showed a sensitivity of 206 $\mu C \cdot Gy_{air}^{-1} \cdot cm^{-2}$ and a dark current drift of 6×10^{-5} $nA \cdot cm^{-1} \cdot s^{-1} \cdot V^{-1}$, which are superior to that of pristine $Cs_2AgBiBr_6$ crystal detectors. Yan et al. [101] developed $MAPbCl_3/MAPbBr_3$ single crystal heterojunction using a space-confined epitaxial method and built a self-powered X-ray detector with a sensitivity of 868 $\mu C \cdot Gy_{air}^{-1} \cdot cm^{-2}$ and low LoD of 15.5 $nGy_{air} \cdot s^{-1}$. This device retained excellent stability even after 120 days in the atmosphere without encapsulation, maintaining over 99% of the initial responsivity.

The high sensitivity, low LoD and fast response enable perovskite X-ray detectors to have high-resolution X-ray imaging. Chen et al. [102] designed a new type of halide perovskite through interlayer-spacing engineering for X-ray detection with high spatial resolution, as shown in Figure 9. A cation (aminoguanidinium, AG^+) with all-NH_2 terminals is designed as the A site in $A_3Bi_2I_9$-type perovskites.

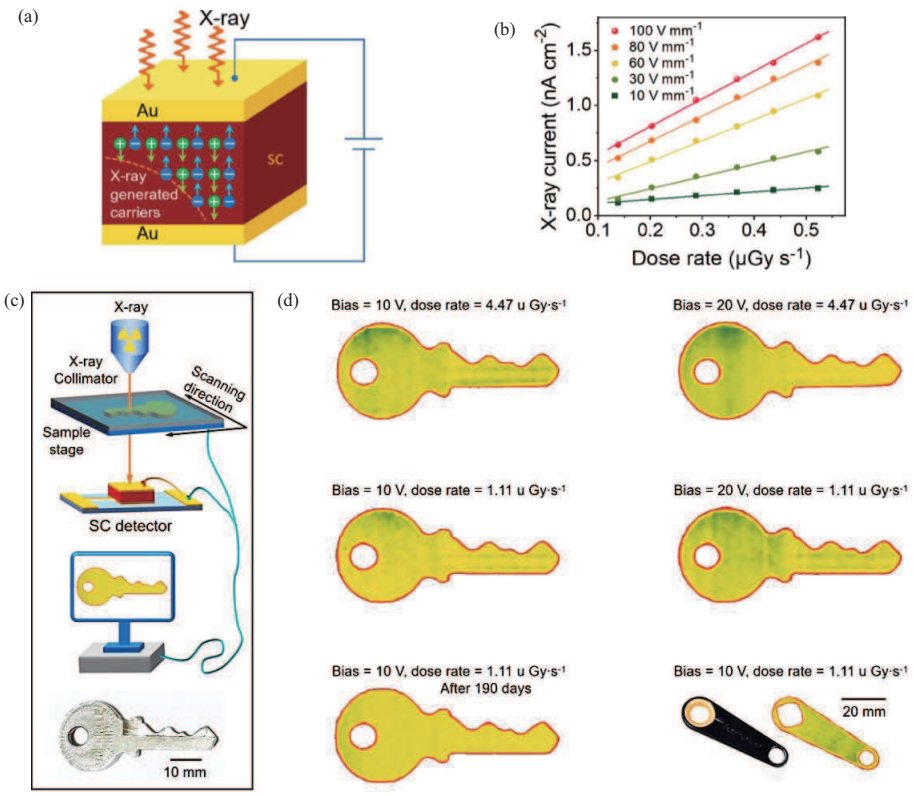

Figure 9 (Color online) High-performance X-ray imaging system using interlayer spacing. (a) Schematic of the X-ray detector structure; (b) the current density of the detector depends on the dose rate at various electric fields; (c) schematic of the X-ray imaging system; (d) X-ray images of a key under different dose rates and bias voltage [102].

The X-ray detectors based on $AG_3Bi_2I_9$ single crystal achieved a high sensitivity of 5791 $\mu C{\cdot}Gy_{air}^{-1}{\cdot}cm^{-2}$, an LoD of 2.6 $nGy_{air}{\cdot}s^{-1}$, and a high spatial resolution of 8.7 $lp{\cdot}mm^{-1}$ at the MTF (modulation transfer function) value of 0.2, offering a promising solution for improved medical diagnostics.

5 Summary

Perovskite photodetectors and high-energy radiation detectors have developed rapidly in the past few years. Single crystal perovskites exhibit engrossing optoelectronic properties that satisfy the major requirements of detectors, such as long carrier lifetime, large carrier diffusion length, wide absorption band range, low trap density, tunable bandgap, and good stability. Significant efforts have been devoted to developing synthetic routes for large-scale, defect-free, single crystalline perovskites, which directly improved the performance of the detector. This review briefly discussed the fundamental principles underlying the photon detection processes and key performance parameters of the X-ray detectors. Additionally, a series of synthetic strategies for preparing single crystal perovskites and recent progress in perovskite X-ray detectors are also overviewed. Notably, the studies presented on perovskite X-ray detectors have achieved performance comparable to or even better than state-of-the-art traditional semiconductor detectors. As shown in Table 3 [11, 16, 28, 57, 78, 79, 86–92, 97, 102–104], the recorded sensitivity has been as high as $\sim 10^8$ $\mu C{\cdot}Gy_{air}^{-1}{\cdot}cm^{-2}$ [103], and the record LoD has been less than 1 $nGy{\cdot}s^{-1}$ [102] to the best of our knowledge. Furthermore, the stability and spatial resolution of perovskite X-ray detectors are satisfactory.

However, further development of perovskite X-ray detectors continues to encounter some challenges. The performance of X-ray detectors considerably depends on the synthesis of perovskites and device preparation. Hence, issues such as thickness control, interface engineering, composition engineering, and large-scale single crystal preparation should be equally important to the detector. For example, latent phase transition during temperature cooling in the ITC method may introduce defects and strains in perovskites [105], harming single crystal quality. The solvent evaporation method is suitable for large-scale preparation but produces relatively poor crystallization quality due to its evaporation rate [106]. Moreover, the reproducibility of perovskite devices that satisfies industrial standards remains a huge

Table 3 Performances and parameters of perovskite single crystal (PSC) for X-ray direct detectors

Material	Device structure	Applied electric field ($V \cdot mm^{-1}$)	Sensitivity ($\mu C \cdot Gy_{air}^{-1} \cdot cm^{-2}$)	Energy	LoD ($nGy_{air} \cdot s^{-1}$)	Dark current drift ($pA \cdot cm^{-1} \cdot s^{-1} \cdot V^{-1}$)	Stability	Ref.
$MAPbBr_3$ (antisolvent)	Au/BCP/C_{60}/PSC/Au	near 0	80	22 keV (up to 50 keV)	~500	–	No EQE loss after air storage for 60 days.	[86]
$Cs_2AgBiBr_6$ (ITC)	Au/PSC/Au	2.5	105 (at a field of 25 V·mm^{-1})	30 keV	59.7	–	Unchanged with a total irradiation dosage of 9257 mG_{air}.	[87]
$MAPbBr_3$ (evaporation)	Si/PSC/C_{60}/BCP/Au	3.5	2.1×10^4 to 8 keV photons	8 keV	< 36	–	–	[78]
$Cs_2AgBiBr_6$ (evaporation with heating)	Ag/PSC/Ag	6	316	39 keV (up to 100 keV)	–	–	–	[28]
$(NH_4)_2Bi_2I_9$ (evaporation with heating)	Ag/PSC/Ag	6.5	8.2×10^3	22 keV (up to 50 keV)	55	–	No obvious current changes after 60 days in ambient air.	[88]
$MAPbBr_3$ (ITC)	Au/PSC/Au	0.83	259.9	39 keV	–	–	–	[11]
$MAPbI_3$ (modified ITC)	Au/PSC/Au	10	–	8 kV	–	–	–	[79]
$Rb_3Bi_2I_9$ (cooling)	Au/PSC/Au	1	42.5	–	8.32	1.82×10^{-4}	Unchanged with a total dose of 5000 Gy, the dark current increased from 1.17 to 9.53 pA with a total dose of 480000 Gy.	[57]
$Cs_3Bi_2I_9$ (evaporation with heating)	Au/PSC/Au	50	1.65×10^3	40 kV	130	–	No noticeable change occurred after 47 days in ambient air.	[89]
$MAPbI_3$ (fast solvent evaporation with inkjet printing)	Au/SC+Graphene/Au	0.167	2.2×10^8	8 keV	–	–	No performance degradation in nine months.	[103]
$FA_{0.85}MA_{0.1}Cs_{0.05}$-$PbI_{2.55}Br_{0.45}$ (ITC)	Au/BCP/C_{60}/PSC/SpiroTTB/Au	60	3.5×10^6	40 kV	42	19	No obvious changes after 60 days in ambient air.	[104]
$MAPbI_3$ (evaporation)	Au/BCP/C_{60}/PSC/MoOx/Au	100	5.2×10^6	22 keV	~0.1	–	Negligible degradation after 1600 h in the air with a humidity of 60%.	[16]
$FA_{0.55}MA_{0.45}PbI_3$ (ITC and seed growth)	ITO/PTAA/PSC/C_{60}/BCP/Cu	0	8.7×10^4	22 keV (up to 50 keV)	27.7	–	Maintain an average 75% performance after 160 h in the open air.	[90]
$MAPbBr_3$ and $CsPbBr_3$ (ITC)	Au/$MAPbBr_3$/$CsPbBr_3$/Au	125	2.0×10^5	120 keV	96	0.39	Retaining 97% of original response after 90 days in ambient conditions.	[91]
$Cs_{0.1}FA_{0.9-z}GA_zPb(I_{0.9}Br_{0.1})_3$: Sr (ITC)	Au/PSC/Au	0.1	2.6×10^4	60 kVp	7.09	0.0877	Reduction in signal current to 10% after 180 days.	[97]
$Cs_3Bi_2Br_9$ (Bridgeman)	Au/PSC/Au	250	1.7×10^3	120 keV	0.58	2.8×10^{-7}	Repeatable performance after 45 days.	[92]
$AG_3Bi_2I_9$ (evaporation with heating)	Au/PSC/Au	100	5.8×10^3	70 to 130 keV	2.6	7.3×10^{-5}	No decay of response with a total dose of 15.43 Gy. Maintain 88% original response value after 120 days in ambient air.	[102]

challenge; almost all the reported devices are fabricated on a lab scale [48]. The toxicity of lead elements found in popular perovskite materials might be another limitation to future applications. Nevertheless, we believe that the remarkable optoelectronic properties of single crystal perovskite X-ray detectors indicate a promising future.

Acknowledgements This work was supported by National Key R&D Program (Grant Nos. 2022YFB3204100, 2021YFC3002200, 2020YFA0709800), National Natural Science Foundation of China (Grant Nos. U20A20168, 51861145202, 61874065, 62022047, 52072204), and XpectVision Technology Co., Ltd. (Grant No. 20212001996). Xiangshun GENG is grateful for the support of the Shuimu Tsinghua Scholar Program.

References

1 Wang S, Yang F, Zhu J, et al. Growth of metal halide perovskite materials. Sci China Mater, 2020, 63: 1438–1463
2 Liu Y, Yang Z, Liu S F. Recent progress in single-crystalline perovskite research including crystal preparation, property evaluation, and applications. Adv Sci, 2018, 5: 1700471
3 Onoda-Yamamuro N, Matsuo T, Suga H. Calorimetric and IR spectroscopic studies of phase transitions in methylammonium trihalogenoplumbates (II)†. J Phys Chem Solids, 1990, 51: 1383–1395
4 Poglitsch A, Weber D. Dynamic disorder in methylammoniumtrihalogenoplumbates (II) observed by millimeter-wave spectroscopy. J Chem Phys, 1987, 87: 6373–6378
5 Mitzi D B. Templating and structural engineering in organic-inorganic perovskites. J Chem Soc Dalton Trans, 2001, 1: 1–12
6 Goldschmidt V M. Die Gesetze der Krystallochemie. Naturwissenschaften, 1926, 14: 477–485
7 Kakavelakis G, Gedda M, Panagiotopoulos A, et al. Metal halide perovskites for high-energy radiation detection. Adv Sci, 2020, 7: 2002098
8 Mao L, Stoumpos C C, Kanatzidis M G. Two-dimensional hybrid halide perovskites: principles and promises. J Am Chem Soc, 2019, 141: 1171–1190
9 Zhang Z, Zhang Z, Zheng W, et al. Sensitive and fast direct conversion X-ray detectors based on single-crystalline HgI_2 photoconductor and ZnO nanowire vacuum diode. Adv Mater Technol, 2020, 5: 1901108
10 Feng Y, Pan L, Wei H, et al. Low defects density $CsPbBr_3$ single crystals grown by an additive assisted method for gamma-ray detection. J Mater Chem C, 2020, 8: 11360–11368
11 Geng X, Feng Q, Zhao R, et al. High-quality single crystal perovskite for highly sensitive X-ray detector. IEEE Electron Dev Lett, 2020, 41: 256–259
12 Abbene L, Gerardi G, Turturici A A, et al. X-ray response of CdZnTe detectors grown by the vertical Bridgman technique: energy, temperature and high flux effects. Nucl Instrum Methods Phys Res Sect A, 2016, 835: 1–12
13 Gao X, Sun H, Yang D, et al. Large-area CdZnTe thick film based array X-ray detector. Vacuum, 2021, 183: 109855
14 Wei H, Huang J. Halide lead perovskites for ionizing radiation detection. Nat Commun, 2019, 10: 1066
15 Zhang Z, Yang G. Recent advancements in using perovskite single crystals for gamma-ray detection. J Mater Sci-Mater Electron, 2021, 32: 12758–12770
16 Song Y, Li L, Hao M, et al. Elimination of interfacial-electrochemical-reaction-induced polarization in perovskite single crystals for ultrasensitive and stable X-ray detector arrays. Adv Mater, 2021, 33: 2103078
17 Lusic H, Grinstaff M W. X-ray-computed tomography contrast agents. Chem Rev, 2013, 113: 1641–1666
18 Saidaminov M I, Adinolfi V, Comin R, et al. Planar-integrated single-crystalline perovskite photodetectors. Nat Commun, 2015, 6: 8724
19 Yu X, Tsao H N, Zhang Z, et al. Miscellaneous and perspicacious: hybrid halide perovskite materials based photodetectors and sensors. Adv Opt Mater, 2020, 8: 2001095
20 Wang P, Zhao Y, Wang T. Recent progress and prospects of integrated perovskite/organic solar cells. Appl Phys Rev, 2020, 7: 031303
21 Cegielski P J, Giesecke A L, Neutzner S, et al. Monolithically integrated perovskite semiconductor lasers on silicon photonic chips by scalable top-down fabrication. Nano Lett, 2018, 18: 6915–6923
22 Li Z, Moon J, Gharajeh A, et al. Room-temperature continuous-wave operation of organometal halide perovskite lasers. ACS Nano, 2018, 12: 10968–10976
23 Das S, Gholipour S, Saliba M. Perovskites for laser and detector applications. Energy Environ Mater, 2019, 2: 146–153
24 Liu G, Jia S, Wang J, et al. Toward microlasers with artificial structure based on single-crystal ultrathin perovskite films. Nano Lett, 2021, 21: 8650–8656
25 Geng X, Zhang P, Ren J, et al. Directly integrated mixed-dimensional van der Waals graphene/perovskite heterojunction for fast photodetection. InfoMat, 2022, 4: e12347
26 Birowosuto M D, Cortecchia D, Drozdowski W, et al. X-ray scintillation in lead halide perovskite crystals. Sci Rep, 2016, 6: 37254
27 Shrestha S, Fischer R, Matt G J, et al. High-performance direct conversion X-ray detectors based on sintered hybrid lead triiodide perovskite wafers. Nat Photon, 2017, 11: 436–440
28 Zhang H, Yang Y, Wang X, et al. X-ray detector based on all-inorganic lead-free $Cs_2AgBiBr_6$ perovskite single crystal. IEEE Trans Electron Dev, 2019, 66: 2224–2229
29 Basiricó L, Ciavatti A, Fraboni B. Solution-grown organic and perovskite X-ray detectors: a new paradigm for the direct detection of ionizing radiation. Adv Mater Technol, 2021, 6: 2000475
30 Yakunin S, Dirin D N, Shynkarenko Y, et al. Detection of gamma photons using solution-grown single crystals of hybrid lead halide perovskites. Nat Photon, 2016, 10: 585–589
31 He Y, Matei L, Jung H J, et al. High spectral resolution of gamma-rays at room temperature by perovskite $CsPbBr_3$ single crystals. Nat Commun, 2018, 9: 1609
32 Zhang Z, Yang G. Recent advancements in using perovskite single crystals for gamma-ray detection. J Mater Sci-Mater Electron, 2021, 32: 12758–12770
33 Onoda-Yamamuro N, Matsuo T, Suga H. Dielectric study of $CH_3NH_3PbX_3$ (X = Cl, Br, I). J Phys Chem Solids, 1992, 53: 935–939
34 Wehrenfennig C, Eperon G E, Johnston M B, et al. High charge carrier mobilities and lifetimes in organolead trihalide perovskites. Adv Mater, 2014, 26: 1584–1589

35 Jeon N J, Noh J H, Yang W S, et al. Compositional engineering of perovskite materials for high-performance solar cells. Nature, 2015, 517: 476–480
36 Dong Q, Fang Y, Shao Y, et al. Electron-hole diffusion lengths > 175 μm in solution-grown $CH_3NH_3PbI_3$ single crystals. Science, 2015, 347: 967–970
37 de Quilettes D W, Vorpahl S M, Stranks S D, et al. Impact of microstructure on local carrier lifetime in perovskite solar cells. Science, 2015, 348: 683–686
38 Stoumpos C C, Malliakas C D, Kanatzidis M G. Semiconducting tin and lead iodide perovskites with organic cations: phase transitions, high mobilities, and near-infrared photoluminescent properties. Inorg Chem, 2013, 52: 9019–9038
39 Xing G, Mathews N, Lim S S, et al. Low-temperature solution-processed wavelength-tunable perovskites for lasing. Nat Mater, 2014, 13: 476–480
40 Zhang Y, Liu Y, Li Y, et al. Perovskite $CH_3NH_3Pb(Br_xI_{1-x})_3$ single crystals with controlled composition for fine-tuned bandgap towards optimized optoelectronic applications. J Mater Chem C, 2016, 4: 9172–9178
41 Miyata A, Mitioglu A, Plochocka P, et al. Direct measurement of the exciton binding energy and effective masses for charge carriers in organic-inorganic tri-halide perovskites. Nat Phys, 2015, 11: 582–587
42 Yin W J, Shi T, Yan Y. Unusual defect physics in $CH_3NH_3PbI_3$ perovskite solar cell absorber. Appl Phys Lett, 2014, 104: 063903
43 Halls J J M, Walsh C A, Greenham N C, et al. Efficient photodiodes from interpenetrating polymer networks. Nature, 1995, 376: 498–500
44 Yakunin S, Sytnyk M, Kriegner D, et al. Detection of X-ray photons by solution-processed lead halide perovskites. Nat Photon, 2015, 9: 444–449
45 Cheng X, Yang S, Cao B, et al. Single crystal perovskite solar cells: development and perspectives. Adv Funct Mater, 2020, 30: 1905021
46 Liu F, Wu R, Zeng Y, et al. Halide perovskites and perovskite related materials for particle radiation detection. Nanoscale, 2022, 14: 6743–6760
47 Su Y, Ma W, Yang Y M. Perovskite semiconductors for direct X-ray detection and imaging. J Semicond, 2020, 41: 051204
48 Zhou X, Wang Y, Ge C, et al. Lead-free perovskite single crystals: a brief review. Crystals, 2021, 11: 1329
49 Zhou F, Li Z, Lan W, et al. Halide perovskite, a potential scintillator for X-ray detection. Small Methods, 2020, 4: 2000506
50 Peng J, Xu Y, Yao F, et al. Thick-junction perovskite X-ray detectors: processing and optoelectronic considerations. Nanoscale, 2022, 14: 9636–9647
51 Wang B, Yang X, Chen S, et al. Flexible perovskite scintillators and detectors for X-ray detection. iScience, 2022, 25: 105593
52 Xu X, Qian W, Xiao S, et al. Halide perovskites: a dark horse for direct X-ray imaging. EcoMat, 2020, 2: e12064
53 Jung G, Ottnad M, Bohnenkamp W, et al. X-ray photoelectron spectroscopy (XPS) of bovine erythrocuprein. FEBS Lett, 1972, 25: 346–348
54 Li S, Xie X, Xiong J, et al. Review: perovskite X-ray detectors (1997-present). Crystals, 2022, 12: 1563
55 Pan L, Shrestha S, Taylor N, et al. Determination of X-ray detection limit and applications in perovskite X-ray detectors. Nat Commun, 2021, 12: 5258
56 IUPAC. Nomenclature, symbols, units and their usage in spectrochemical analysis-XI. Detection of radiation (IUPAC Recommendations 1995). Spectrochim Acta Part B: Atomic Spectrosc, 1997, 52: 539–552
57 Xia M, Yuan J, Niu G, et al. Unveiling the structural descriptor of $A_3B_2X_9$ perovskite derivatives toward X-ray detectors with low detection limit and high stability. Adv Funct Mater, 2020, 30: 1910648
58 Sun K, Tan D, Fang X, et al. Three-dimensional direct lithography of stable perovskite nanocrystals in glass. Science, 2022, 375: 307–310
59 Zhang J, Li C, Liang Y, et al. Solution-processed selective area homoepitaxial growth of suspended $MAPbX_3$ (X = Cl, Br) perovskite micro-arrays. Adv Funct Mater, 2023, 33: 2208841
60 Chen S, Xiao X, Chen B, et al. Crystallization in one-step solution deposition of perovskite films: upward or downward? Sci Adv, 2021, 7: 2412
61 Gu Z, Huang Z, Li C, et al. A general printing approach for scalable growth of perovskite single-crystal films. Sci Adv, 2018, 4: 2390
62 Günzler A, Bermúdez-Ureña E, Muscarella L A, et al. Shaping perovskites: in situ crystallization mechanism of rapid thermally annealed, prepatterned perovskite films. ACS Appl Mater Interfaces, 2021, 13: 6854–6863
63 Corzo D, Wang T, Gedda M, et al. A universal cosolvent evaporation strategy enables direct printing of perovskite single crystals for optoelectronic device applications. Adv Mater, 2022, 34: 2109862
64 Xiao M, Huang F, Huang W, et al. A fast deposition-crystallization procedure for highly efficient lead iodide perovskite thin-film solar cells. Angew Chem Int Ed, 2014, 53: 9898–9903
65 Jeon N J, Noh J H, Kim Y C, et al. Solvent engineering for high-performance inorganic-organic hybrid perovskite solar cells. Nat Mater, 2014, 13: 897–903
66 Zhu Z, Deng W, Li W, et al. Antisolvent-induced fastly grown all-inorganic perovskite $CsPbCl_3$ microcrystal films for high-sensitive UV photodetectors. Adv Mater Inter, 2021, 8: 2001812
67 Zhang L, Zhang J, Shang Q, et al. Ultrafast antisolvent growth of single-crystalline $CsPbCl_3$ microcavity for low-threshold room temperature blue lasing. ACS Appl Mater Interfaces, 2022, 14: 21356–21362
68 Shi D, Adinolfi V, Comin R, et al. Low trap-state density and long carrier diffusion in organolead trihalide perovskite single crystals. Science, 2015, 347: 519–522
69 Cha J H, Han J H, Yin W, et al. Photoresponse of $CsPbBr_3$ and Cs_4PbBr_6 perovskite single crystals. J Phys Chem Lett, 2017, 8: 565–570
70 Rakita Y, Kedem N, Gupta S, et al. Low-temperature solution-grown $CsPbBr_3$ single crystals and their characterization. Cryst Growth Des, 2016, 16: 5717–5725
71 Tavakoli M M, Yadav P, Prochowicz D, et al. Controllable perovskite crystallization via antisolvent technique using chloride additives for highly efficient planar perovskite solar cells. Adv Energy Mater, 2019, 9: 1803587
72 Zuo C, Ding L. Lead-free perovskite materials $(NH_4)_3Sb_2I_xBr_{9-x}$. Angew Chem Int Ed, 2017, 56: 6528–6532
73 Kim J, Yun J S, Cho Y, et al. Overcoming the challenges of large-area high-efficiency perovskite solar cells. ACS Energy Lett, 2017, 2: 1978–1984
74 Peng S Y, Chuang K W, He J H, et al. Direct growth and patterning of single-crystal perovskites via antisolvent inkjet printing. ACS Appl Electron Mater, 2022, 4: 5468–5474
75 Kadro J M, Nonomura K, Gachet D, et al. Facile route to freestanding $CH_3NH_3PbI_3$ crystals using inverse solubility. Sci

Rep, 2015, 5: 11654
76 Saidaminov M I, Abdelhady A L, Murali B, et al. High-quality bulk hybrid perovskite single crystals within minutes by inverse temperature crystallization. Nat Commun, 2015, 6: 7586
77 Liu Y, Yang Z, Cui D, et al. Two-inch-sized perovskite CH3NH3PbX3 (X = Cl, Br, I) crystals: growth and characterization. Adv Mater, 2015, 27: 5176–5183
78 Wei W, Zhang Y, Xu Q, et al. Monolithic integration of hybrid perovskite single crystals with heterogenous substrate for highly sensitive X-ray imaging. Nat Photon, 2017, 11: 315–321
79 Wang W, Meng H, Qi H, et al. Electronic-grade high-quality perovskite single crystals by a steady self-supply solution growth for high-performance X-ray detectors. Adv Mater, 2020, 32: 2001540
80 Gao L, Tao K, Sun J, et al. Gamma-ray radiation stability of mixed-cation lead mixed-halide perovskite single crystals. Adv Opt Mater, 2022, 10: 2102069
81 May A F, Yan J, McGuire M A. A practical guide for crystal growth of van der Waals layered materials. J Appl Phys, 2020, 128: 051101
82 Zhang P, Hua Y, Li X, et al. Filter-free color image sensor based on $CsPbBr_{3-3n}X_{3n}$ (X = Cl, I) single crystals. J Mater Chem C, 2021, 9: 2840–2847
83 Zhou F, Li Z, Lan W, et al. Halide perovskite, a potential scintillator for X-ray detection. Small Methods, 2020, 4: 2000506
84 Zhang Z, Dierks H, Lamers N, et al. Single-crystalline perovskite nanowire arrays for stable X-ray scintillators with micrometer spatial resolution. ACS Appl Nano Mater, 2022, 5: 881–889
85 Pan Z, Wu L, Jiang J, et al. Searching for high-quality halide perovskite single crystals toward X-ray detection. J Phys Chem Lett, 2022, 13: 2851–2861
86 Wei H, Fang Y, Mulligan P, et al. Sensitive X-ray detectors made of methylammonium lead tribromide perovskite single crystals. Nat Photon, 2016, 10: 333–339
87 Pan W, Wu H, Luo J, et al. $Cs_2AgBiBr_6$ single-crystal X-ray detectors with a low detection limit. Nat Photon, 2017, 11: 726–732
88 Zhuang R, Wang X, Ma W, et al. Highly sensitive X-ray detector made of layered perovskite-like $(NH_4)_3Bi_2I_9$ single crystal with anisotropic response. Nat Photon, 2019, 13: 602–608
89 Zhang Y, Liu Y, Xu Z, et al. Nucleation-controlled growth of superior lead-free perovskite $Cs_3Bi_2I_9$ single-crystals for high-performance X-ray detection. Nat Commun, 2020, 11: 2304
90 Wu J, Wang L, Feng A, et al. Self-powered $FA_{0.55}MA_{0.45}PbI_3$ single-crystal perovskite X-ray detectors with high sensitivity. Adv Funct Mater, 2021, 32: 2109149
91 Cui F, Zhang P, Zhang L, et al. Liquid-phase epitaxial growth of large-area $MAPbBr_{3-n}Cl_n/CsPbBr_3$ perovskite single-crystal heterojunction for enhancing sensitivity and stability of X-ray detector. Chem Mater, 2022, 34: 9601–9612
92 Li X, Zhang P, Hua Y, et al. Ultralow detection limit and robust hard X-ray imaging detector based on inch-sized lead-free perovskite $Cs_3Bi_2Br_9$ single crystals. ACS Appl Mater Interfaces, 2022, 14: 9340–9351
93 Pang J, Zhao S, Du X, et al. Vertical matrix perovskite X-ray detector for effective multi-energy discrimination. Light Sci Appl, 2022, 11: 105
94 Peng W, Miao X, Adinolfi V, et al. Engineering of $CH_3NH_3PbI_3$ perovskite crystals by alloying large organic cations for enhanced thermal stability and transport properties. Angew Chem Int Ed, 2016, 55: 10686–10690
95 Kishimoto T, Suzuki A, Ueoka N, et al. Effects of guanidinium addition to $CH_3NH_3PbI_{3-x}Cl_x$ perovskite photovoltaic devices. J Ceram Soc Jpn, 2019, 127: 491–497
96 Pei Y, Liu Y, Li F, et al. Unveiling property of hydrolysis-derived $DMAPbI_3$ for perovskite devices: composition engineering, defect mitigation, and stability optimization. iScience, 2019, 15: 165–172
97 Jiang J, Xiong M, Fan K, et al. Synergistic strain engineering of perovskite single crystals for highly stable and sensitive X-ray detectors with low-bias imaging and monitoring. Nat Photon, 2022, 16: 575–581
98 Li Z, Chen Y, Zhang C, et al. Phenyl-terminated coupling interface enabled highly efficient and stable multiwavelength perovskite single crystal/silicon integrated photodetector. ACS Appl Mater Interfaces, 2023, 15: 17377–17385
99 Li Z, Huang S, Chen Y, et al. Vapor-deposited amino coupling of hybrid perovskite single crystals and silicon wafers toward highly efficient multiwavelength photodetection. ACS Appl Mater Interfaces, 2022, 14: 52476–52485
100 Zhang X, Zhu T, Ji C, et al. In situ epitaxial growth of centimeter-sized lead-free $(BA)_2CsAgBiBr_7/Cs_2AgBiBr_6$ heterocrystals for self-driven X-ray detection. J Am Chem Soc, 2021, 143: 20802–20810
101 Yan J, Gao F, Tian Y, et al. Controllable perovskite single crystal heterojunction for stable self-powered photo-imaging and X-ray detection. Adv Opt Mater, 2022, 10: 2200449
102 Chen M, Dong X, Chu D, et al. Interlayer-spacing engineering of lead-free perovskite single crystal for high-performance X-ray imaging. Adv Mater, 2023, 35: 2211977
103 Glushkova A, Andričević P, Smajda R, et al. Ultrasensitive 3D aerosol-jet-printed perovskite X-ray photodetector. ACS Nano, 2021, 15: 4077–4084
104 Liu Y, Zhang Y, Zhu X, et al. Triple-cation and mixed-halide perovskite single crystal for high-performance X-ray imaging. Adv Mater, 2021, 33: 2006010
105 Chen Y, Lei Y, Li Y, et al. Strain engineering and epitaxial stabilization of halide perovskites. Nature, 2020, 577: 209–215
106 Li J, Han Z, Gu Y, et al. Perovskite single crystals: synthesis, optoelectronic properties, and application. Adv Funct Mater, 2021, 31: 2008684